

PAPER

## Divertor leg filaments in NSTX-U

To cite this article: Filippo Scotti *et al* 2018 *Nucl. Fusion* **58** 126028

View the [article online](#) for updates and enhancements.

# Divertor leg filaments in NSTX-U

Filippo Scotti<sup>1</sup>, Stewart Zweben<sup>2</sup>, Vlad Soukhanovskii<sup>1</sup>, Derek Baver<sup>3</sup>  
and James Myra<sup>3</sup>

<sup>1</sup> Lawrence Livermore National Laboratory, Livermore, CA 94550, United States of America

<sup>2</sup> Princeton Plasma Physics Laboratory, Princeton, NJ 08540, United States of America

<sup>3</sup> Lodestar Research Corporation, Boulder, CO 80301, United States of America

E-mail: [fscotti@pppl.gov](mailto:fscotti@pppl.gov)

Received 30 August 2018

Accepted for publication 27 September 2018

Published 24 October 2018



## Abstract

This paper presents the first observation of divertor localized turbulence in the NSTX-Upgrade spherical tokamak. Previous work in NSTX discharges (Maqueda *et al* 2010 *Nucl. Fusion* **50** 075002) described fluctuations on the divertor target due to blobs generated on the low field side midplane. In the region that shows disconnection from upstream turbulence (private flux region and proximity of the strike point), divertor-localized fluctuations are observed via imaging of C III and D- $\alpha$  emission in diverted L-mode discharges and are characterized in this paper. Field-aligned filaments connected to the divertor target plate are radially localized at the separatrix on the outer divertor leg and in the private flux region on the inner divertor leg. These are limited to the region below the X-point with fluctuation levels up to 10%–20%. The filaments have comparable poloidal and radial correlation lengths (10–100 ion gyroradii  $\rho_i$ ) and parallel correlation lengths of several meters. Toroidal mode numbers are in the range of 10–30 and 2–10 for outer and inner leg filaments. The poloidal motion of outer leg filaments has the same direction and comparable magnitude to advection due to  $E \times B$  drift calculated by the multi-fluid edge transport code UEDGE with inclusion of cross field drifts. Disconnection between inner and outer leg filaments as well as the absence of correlation with upstream turbulence support the hypothesis of X-point disconnection for divertor leg filaments. Simulations with the ArbiTER linear eigenvalue solver and a resistive-ballooning model were performed with a simulation grid limited to the divertor legs. Instabilities localized to the bad curvature side of the divertor legs were observed, in qualitative agreement with the experiment.

Keywords: turbulence, divertor, plasma imaging, scrape-off layer

(Some figures may appear in colour only in the online journal)

## 1. Introduction

A narrow scrape-off layer (SOL) heat flux width  $\lambda_q$  will represent a challenge for wall materials in fusion reactors. The multi-machine database [2] and the heuristic drift model for the power scrape-off width [3] project to a sub-mm  $\lambda_q$  in ITER. Recent simulations with the XGC-1 code [4] predict larger  $\lambda_q$  ( $\sim 5$  mm) in ITER, due to a transition from neoclassical to turbulence-dominated  $\lambda_q$ .

SOL turbulence [5] can contribute to the heat and particle fluxes to the first wall and divertor plate in tokamaks [6]. Clarifying the three dimensional (3D) structure of SOL and divertor turbulence and its scaling with plasma parameters is therefore critical for the understanding and extrapolation of

divertor heat fluxes as well as for the interpretation of divertor transport and radiation, usually based on average quantities.

On the low field side (LFS) midplane of toroidal plasma devices, SOL turbulence, due to drift waves and interchange instabilities, has been characterized in multiple machines [5] and is known to have parallel and perpendicular scale lengths of many meters and a few centimeters, respectively. However, it has not been clear until recently to what extent SOL turbulence extends to the divertor plate, or whether there is any additional turbulence generated in the divertor region itself. Divertor turbulence has been investigated via active/passive imaging and Langmuir probes in several devices [1, 7–11] and divertor filamentary structures were generally interpreted as the divertor extension of midplane blobs.

X-point disconnection of turbulent filaments due to collisionality and magnetic geometry has been discussed in theoretical papers [12, 13]. Parallel connection of outer midplane turbulence to the divertor was characterized in the National Spherical Torus Experiment (NSTX) [1] and Alcator C-Mod [8] via cross correlation of blobs measured via the gas puff imaging diagnostic (GPI) [14] and divertor fluctuations measured via imaging and probes. NSTX results showed a loss of correlation approaching the strike point [1]. Passive imaging of the lower divertor in the Mega Ampere Spherical Tokamak (MAST) showed a reduction in fluctuations approaching the separatrix [15].

Along with divertor fluctuations due to midplane turbulence, divertor-localized fluctuations could enhance the spreading of particle and heat fluxes near the separatrix. Recently, intermittent filaments in the *divertor legs* have been observed in multiple tokamaks. *Divertor leg* here indicates the region below the X-point and radially limited to a few cm around the separatrix in both common and private flux regions. Divertor leg filaments were studied in the private flux region of the inner divertor leg via visible fast camera imaging from a tangential viewport in MAST [7]. Similar filaments were observed in the C-Mod divertor via imaging of deuterium Balmer- $\alpha$  ( $D\alpha$ ) emission [16].

Theoretical papers have studied the possibility of divertor-localized fluctuations; however, the relationship of these models to the recent experimental measurements has not yet been established. Fluctuations resulting from radial electron temperature gradient  $\nabla T_e$  and sheath boundary conditions were conjectured for tokamak SOL plasma [17, 18].  $\nabla T_e$ -driven flute-like instabilities limited to the region between the divertor plate and the X-point were then considered, with X-point disconnection discussed in this context as a mechanism to limit instabilities to the divertor region [13, 19]. Dispersion relations were derived and geometry effects were considered for growth rates, dynamics and mode localization [20–22].

This paper presents the first observation in the National Spherical Torus eXperiment Upgrade (NSTX-U) [23] of divertor fluctuations localized on the divertor legs and limited to the divertor region. Statistical properties, spatial/temporal scales and filament motion are characterized as a step towards the identification of these instabilities. The paper is organized as follows: SOL flux tube structure in section 2, experimental setup in section 3, interpretation of divertor filamentary fluctuations in section 4, 2D filaments cross correlations in section 5, filament motion in section 6, correlation with midplane turbulence in section 7 and scaling with plasma parameters in section 8. Sections 9 and 10 present discussion and conclusions.

## 2. SOL flux tube structure in the NSTX-U divertor

Given the rapid motion of electrons along a field line, the spatial structure of divertor turbulence can be visualized from the field line mapping of flux tubes with an originating point in the LFS midplane (for midplane blobs) and in the divertor region (for divertor-localized modes). Figure 1 shows renderings (performed with the ray tracing code POV-Ray [24]) of flux tubes in the NSTX-U divertor for discharge 205020. The

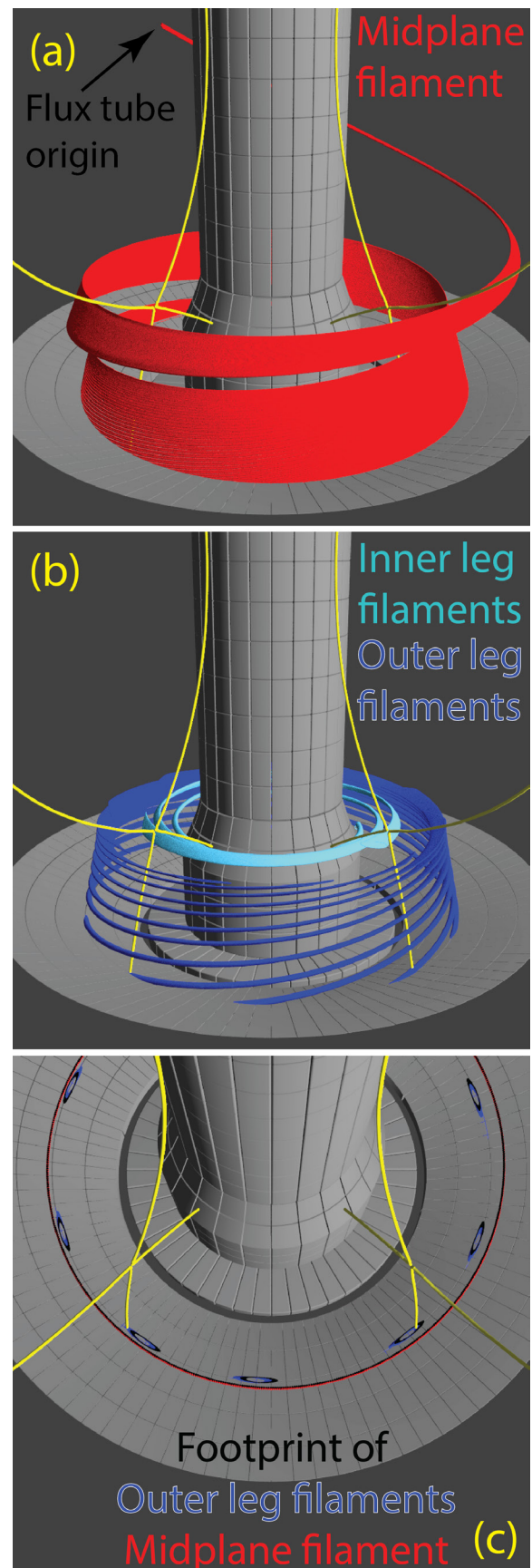


**Figure 1.** Rendering of the NSTX-U divertor with flux tubes corresponding to a midplane blob (a), divertor-localized fluctuations (b) and their intersection with the divertor floor (c). The separatrix is rendered in yellow at two toroidal locations.

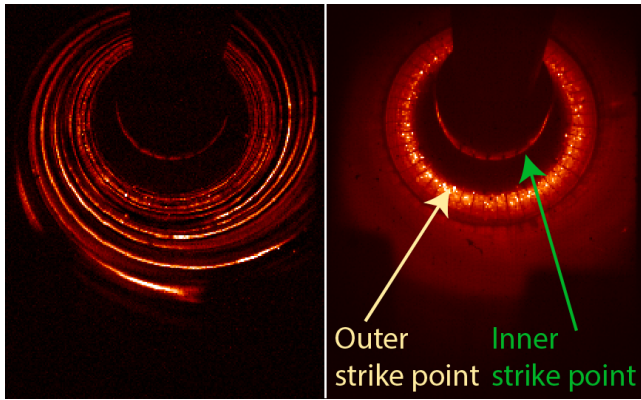


**Figure 2.** Li I imaging of divertor fluctuations in NSTX: fluctuating (left) and average (right) components.

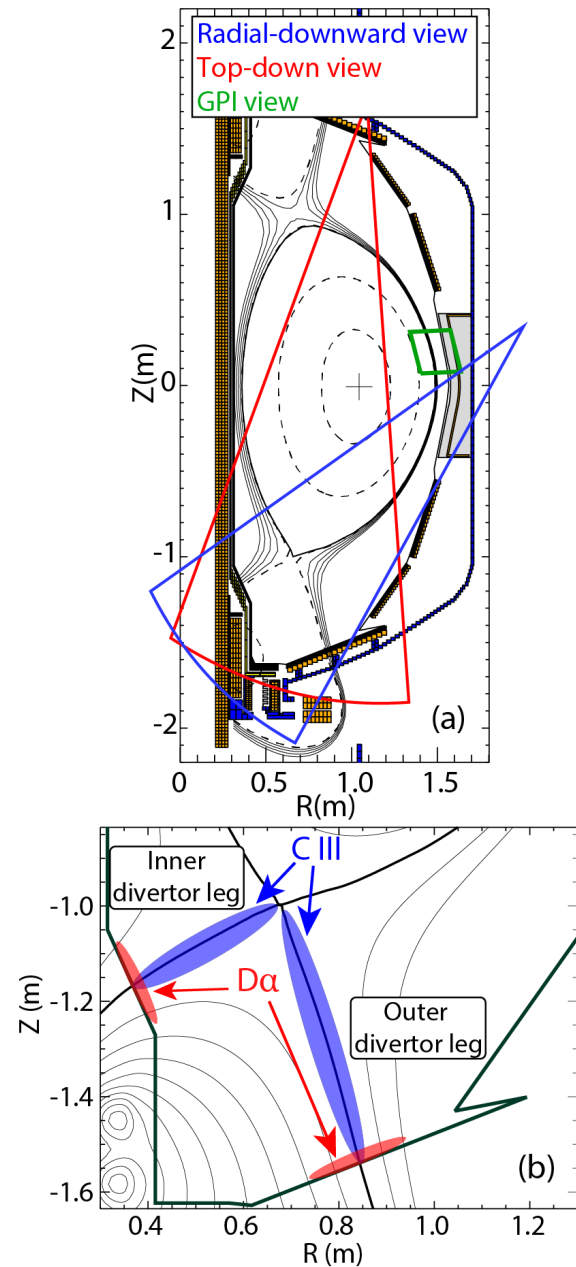
equilibrium reconstruction is generated by the EFIT02 code and flux tubes are created following magnetic field lines. The separatrix is shown in yellow at two toroidal locations.

Figure 1(a) shows the field line mapping of a midplane blob (flux tube with a circular cross section at midplane, 1 cm in radius, 4 mm outside the separatrix) in red. Flux expansion and magnetic shear squeeze the circular flux tube to a ribbon-like cross section in the divertor region. Figure 1(b) shows in cyan the structure of three inner divertor leg filaments and in blue the structure of ten outer leg filaments obtained via field line mapping of circular flux tubes in the private flux region of the inner leg and on the outer leg separatrix, respectively. Figure 1(c) shows the *footprint* of these filamentary structures (i.e. the intersection with the divertor plate), limiting the combined rendering of figures 1(a) and (b) to 1 cm of the divertor floor and moving to a top-down view. Midplane blobs intersect the divertor plate with a spiral footprint while divertor leg-localized filaments have elliptical footprints.

The difference in shape and spatial localization of these flux tubes can be used to distinguish turbulence originating at midplane and extending in the divertor from turbulence originating on the divertor legs. Passive imaging via different emitting species (different elements or different charge states) can isolate fluctuations in separate  $T_e$  regions and sample distinct radial or poloidal divertor zones e.g. to image the poloidal structure or the filaments intersection with the divertor plate. As an example, passive divertor imaging via neutral lithium emission (localized on the divertor surface due to the short ionization mean free path) [25] enabled imaging of the helical divertor footprint of midplane turbulence in NSTX. Figure 2 shows Li I emission from the top-down view: fluctuating (left) and mean (right) component. The spiral structures are caused by filaments generated upstream (see figure 1(a)) while their surface localization is controlled by the emission of the monitored species. Imaging of divertor leg filaments (i.e. as in figure 1(b)) will require emission localized at higher  $T_e$  and is discussed in section 3.

### 3. Experimental setup and method

The results in this paper are from the first NSTX-U experimental campaign [26–28]. NSTX-U is the upgrade to the



**Figure 3.** (a) NSTX-U equilibrium reconstruction with overlay of diagnostic fields of view: radial downward view (blue), top-down view (red), midplane field-aligned view (green); (b) close-up of the divertor with schematic of C III and D- $\alpha$  emission regions.

NSTX tokamak, with a new center stack (doubling the toroidal field  $B_T$  up to 1 T and the plasma current  $I_p$  up to 2 MA) and the addition of a second neutral beam (doubling the input power  $P_{NBI}$  to 15 MW). The discharges analyzed in this paper are NBI-heated (1.5–3.5 MW) L-mode lower single null or double null discharges ( $\delta_{r-sep} = 0-4$  mm) with weak shaping and long divertor legs (elongation  $\kappa = 1.7$ , triangularity  $\delta = 0.47$ , X-point height  $Z_X = 0.6$  m) as shown in figure 3. The  $B \times \nabla B$  direction was towards the lower divertor.

In NSTX-U discharges with attached divertor plasma conditions, the C III emission at 465 nm (associated with  $T_e \sim 5-10$  eV [29]) was localized to the divertor legs and was a candidate for the imaging of divertor leg fluctuations. C III

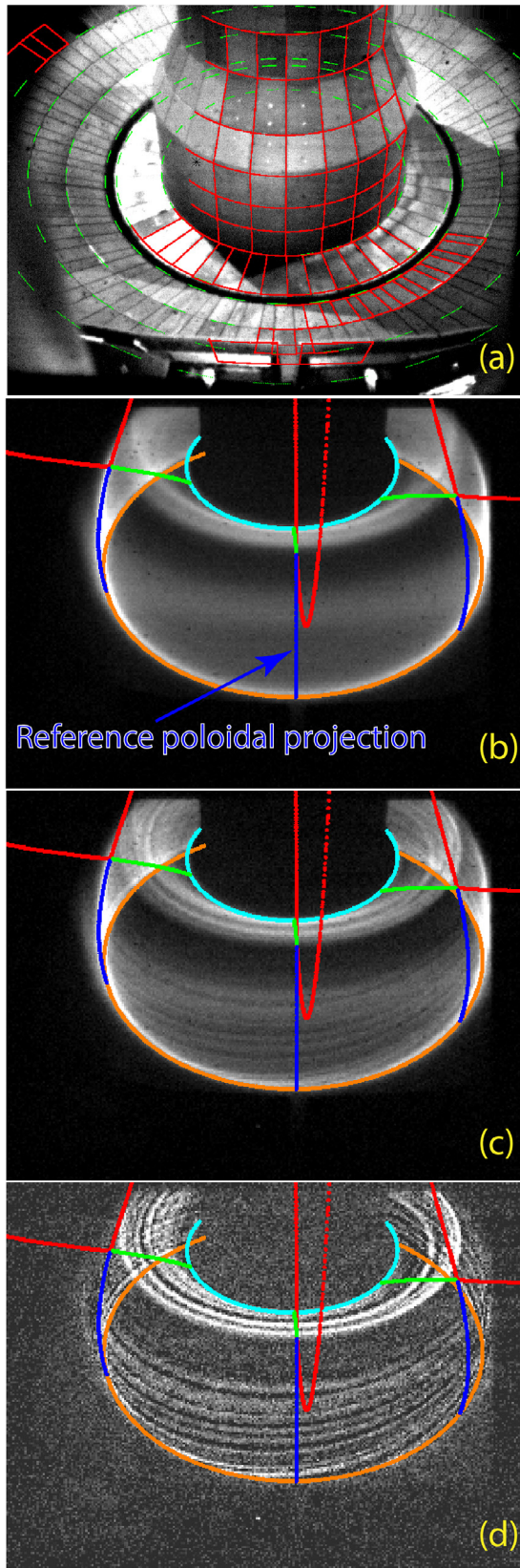


**Figure 4.** (a) Image of the lower divertor from the radial-downward view, (b) C III emission averaged over 1 ms; (c) raw frame ( $9.3 \mu\text{s}$  exposure); (d) raw frame after high pass filter. Separatrix (red), inner (green) and outer (blue) divertor legs, inner (cyan) and outer (orange) strike points are overlaid.

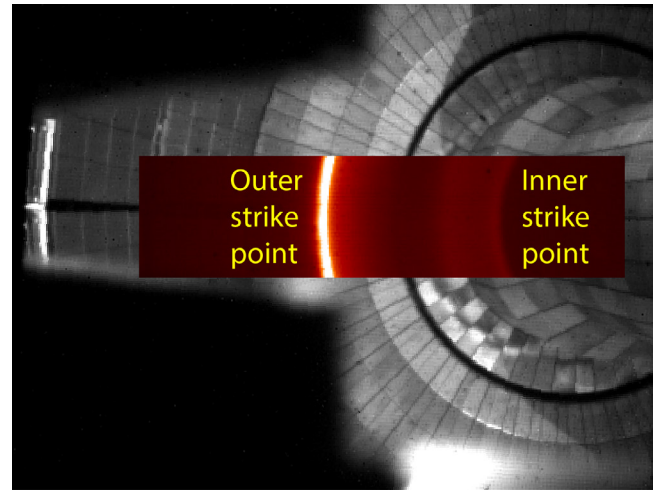


**Figure 5.** Image of the lower divertor from the top-down view. A D- $\alpha$  image from the cropped view is overlaid.

emission is typically about  $10\times$  less bright than D- $\alpha$  or Li I emission. A new imaging setup was implemented with a more sensitive camera and optimized throughput. A Vision Research [30] Phantom v1211 fast CMOS camera was utilized. The camera has  $1280 \times 800$  square  $28 \mu\text{m}$  pixels, 12 bit digitization and is five times more sensitive than the Phantom v710 used in NTSX for GPI and passive divertor imaging [1, 25]. A coherent fiber bundle ( $1000 \times 800$   $10 \mu\text{m}$  fibers) was used to relay the image to the camera where optics optimized for throughput (collimating  $f = 85 \text{ mm } F/1.4$ , focus  $f = 50 \text{ mm } F/1.2$ ) provided a 1:1.7 imaging on the detector. The setup enabled imaging at up to 140 kHz at a resolution of  $272 \times 192$  pixels (generally limited by available light). A 3 inch narrow bandpass filter (Andover [31],  $\Delta\lambda \sim 10.0 \text{ nm}$  in full width at half maximum FWHM) with peak transmission  $\sim 0.75$  was used to isolate C III emission. Other transition lines (i.e. C IV, He II) within the bandpass did not contribute more than a few % of the collected light. The field of view is shown in blue in figure 3(a), overlaid to an NSTX-U equilibrium reconstruction. A close-up of the divertor in figure 3(b) shows in blue the typical C III emission region around the divertor legs.

In order to interpret 3D fluctuating structures from this radial-downward view, a synthetic diagnostic was developed using the interactive data language (IDL) code [32]. Coordinates of the plasma facing components (PFCs) were obtained from in-vessel metrology. The camera view was reconstructed in IDL and the rectilinear projection of the PFCs onto the detector was calculated. The camera angle and focal length were adjusted until a match between the calibration image and the reconstructed PFCs was obtained, with an accuracy on the order of 1 cm. Figure 4(a) shows the calibration image acquired with in-vessel illumination. The projection of the reconstructed PFCs measured with the metrology arm is overlaid with red lines. Dashed green lines represent the projection of the PFCs not directly measured but extrapolated from the measurements at a different toroidal location.

The synthetic diagnostic enabled the overlay of 3D structures such as the separatrix or field lines onto the acquired

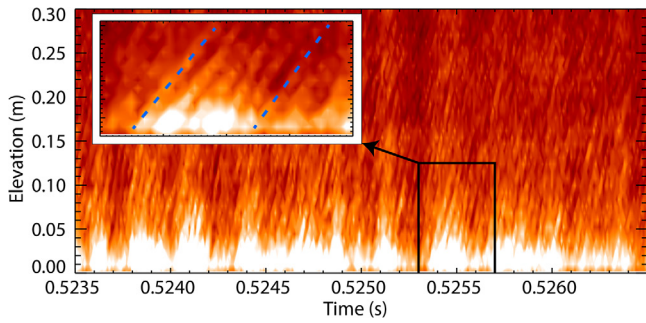


**Figure 6.** C III emission along the outer divertor leg versus time and poloidal elevation from the strike point. Details of filaments trajectories are shown in the inset.

images and the creation of poloidal/toroidal reference projections that were used for the interpretation of fluctuation characteristics. Figure 4(b) shows an image of the lower divertor C III emission averaged over 1 ms. Projection of the separatrix (red), inner (green) and outer (blue) divertor legs, inner (cyan) and outer (orange) strike points from the EFIT02 reconstruction are overlaid at three toroidal locations. Figure 4(c) shows a raw frame acquired at 100 kHz ( $9.3 \mu\text{s}$  exposure). Filamentary structures corresponding to the flux tubes shown in figure 1(b) are observed on both divertor legs in the raw image. The contrast of these structures is enhanced in figure 4(d) with a moving minimum subtraction over  $\pm 100 \mu\text{s}$ .

Two other cameras completed the imaging diagnostic suite used in this work. The first was a Vision Research Phantom v710 fast camera filtered for D- $\alpha$  emission with a wide-angle top-down view of the lower divertor [25]. The field of view is shown in figure 5 while the PFCs were illuminated by the in-vessel filaments. A crop of the full field of view was used limiting the toroidal extent to enable higher framing rates. A resolution of  $256 \times 64$  pixels was employed with a 280 kHz frame rate and  $3 \mu\text{s}$  exposure. Raw D- $\alpha$  emission from the cropped view is overlaid onto the full field of view. Emission at the inner strike point (ISP) and at the outer strike point (OSP) can be observed. The D- $\alpha$  emission is poloidally localized to the proximity of the strike point (as in figure 3(b)) and will be employed for the analysis of the footprint of divertor fluctuations. The second additional camera is a Vision Research Phantom v710 camera looking at the LFS midplane passive D- $\alpha$  emission with a field aligned view via the GPI optics [33]. Upstream D- $\alpha$  emission was acquired at 100 kHz framing rate with a  $9 \mu\text{s}$  exposure. The fields of view of these cameras are shown in figure 3: green box for upstream D- $\alpha$  and red region for the top-down D- $\alpha$  view.

#### 4. Statistics of divertor-leg filaments

General properties (appearance, statistics, time scales) of inner and outer leg divertor filaments are presented in this section. Figure 4(b) showed the average C III emission in the NSTX-U divertor. C III emission is localized radially around the separatrix location and poloidally to the entire inner divertor leg and most of the outer leg (see blue shaded region in figure 3(b)), thus highlighting the region of interest for the

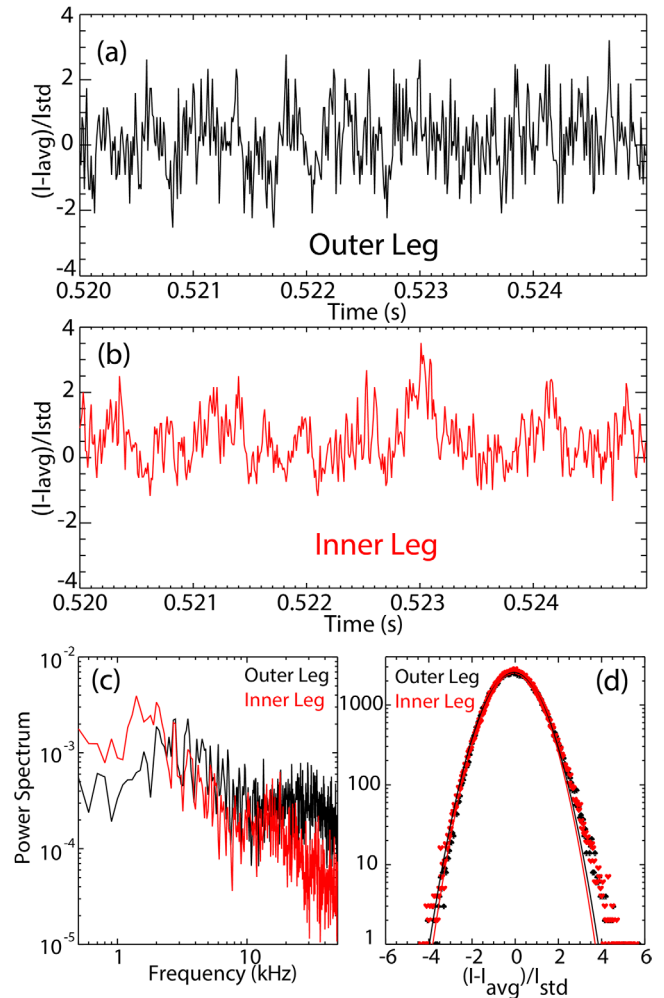


**Figure 7.** ((a) and (b)) Time histories of a pixel in the outer and inner divertor legs, (c) power spectra and (d) PDFs for inner and outer divertor leg fluctuations.

study of divertor leg modes (as rendered in figure 1(b)). In figure 4(d), several filamentary structures can be observed on both inner and outer legs. These intermittent filaments in light emission are assumed to be representative of  $n_e$  fluctuations (appendix) and have helical shapes approximately following field lines, with typical size across the field much shorter than along the field ( $k_{\perp} \gg k_{\parallel}$ ).

C III emission from this view is interpolated onto a projection of the outer divertor leg (blue reference curve in figure 4(b)). Figure 6 shows the contour plot of the raw C III emission along the outer divertor leg as a function of time and poloidal distance from the strike point. Filamentary structures are observed at frequencies  $\sim 10$ – $30$  kHz. Filaments show an upward movement (towards the X-point) and can be followed for  $50$ – $100 \mu\text{s}$ . An axisymmetric modulation at a few kHz of the divertor emission is also observed but related to upstream modes.

Time histories of a single pixel after subtraction of the mean and normalization by the standard deviation are shown in figures 7(a) and (b) for a pixel in the outer divertor leg and for a pixel in the inner divertor leg, respectively. Fluctuation levels inferred from the root-mean-squared (RMS) fluctuations

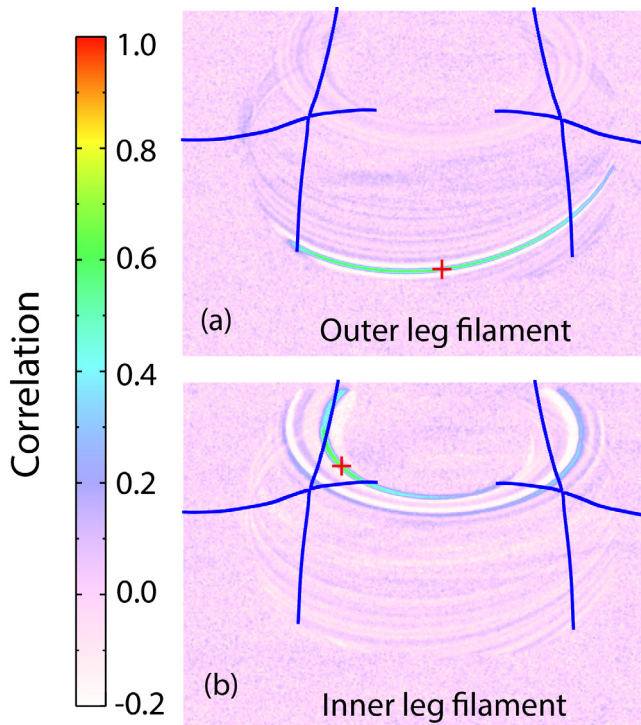


**Figure 8.** 2D cross correlation maps for outer (a) and inner (b) leg filaments. The reference pixel for the 2D cross correlation is indicated with a red cross.

normalized by the average counts are up to 10%–20%. Fluctuation levels due to divertor leg filaments are on the order of 2.5–9 times the single pixel noise level. Figure 7(c) shows power spectra for outer and inner leg fluctuations indicating broadband fluctuations with characteristic frequencies on the order of 10 kHz for inner leg filaments and 20–30 kHz for outer leg filaments. Probability density functions (PDFs) for inner and outer divertor leg fluctuations are shown in figure 7(d), with similar near-Gaussian PDFs. Gaussian fits to the PDFs are also overlaid, indicating a small positive skewness to the experimental PDFs.

Characteristic time scales for the divertor leg filaments are inferred from the auto-correlation of single pixel time series on the inner and outer legs. The auto-correlation time  $\tau_{\text{corr}}$  (inferred from the FWHM of the auto correlation function) is  $\sim 10$ – $30 \mu\text{s}$  for outer leg filaments and  $30$ – $100 \mu\text{s}$  for inner leg filaments. In order to take into account the effect of poloidal/toroidal filament motion, the maximum of the time delayed cross correlation as a function of delay was evaluated for pixels within a few cm across the direction of motion, leading to an estimate of up to  $\sim 50 \mu\text{s}$  for the lifetime of outer leg filaments.

## 5. 2D filament cross correlations

Filaments spatial structure is inferred from the zero-delay 2D cross correlations maps of the time series of a reference pixel with that of each other pixel in the camera view. Time series of 5 ms are utilized while a high-pass filter at a 8 kHz is used to filter-out the low frequency axisymmetric modulation in

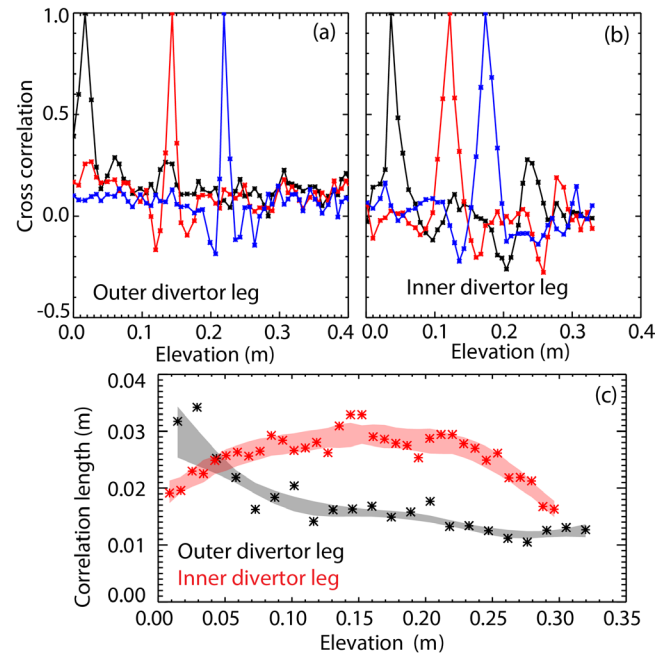


**Figure 9.** Poloidal correlation function for outer (a) and inner (b) leg filaments at different elevations, (c) poloidal correlation lengths as a function of poloidal distance along the outer and inner divertor legs.

divertor emission (as in figure 6). Pixels corresponding to different elevations and radial locations on both the inner and the outer divertor legs are taken as the reference point for the 2D correlation maps. Spatial cross correlations are calculated for both divertor cameras discussed in the previous section (C III and D- $\alpha$ ) to determine radial ( $L_{\text{rad}}$ ), poloidal ( $L_{\text{pol}}$ ) and parallel ( $L_{\parallel}$ ) correlation lengths. Since the two cameras are looking at different emitting species, the different localization of the emission along the same fluctuating structures allows for complimentary quantities to be extracted. Time-delayed cross correlations are discussed in section 6.

### 5.1. Poloidal filament structure

Poloidal and parallel correlation lengths as well as effective toroidal mode numbers are inferred from the radial-downward view (see figure 3(b) for the typical C III emission and figure 4 for the camera field of view), interpolating the 2D cross correlation maps onto poloidal and toroidal pixel projections of the camera view. Figure 8 shows contour plots of the 2D cross correlation function for a reference pixel in the outer leg (a) and a pixel in the inner leg (b) at an elevation of 10 cm above the strike point along the divertor leg. The value of each pixel in the correlation maps ( $272 \times 192$  pixels) represents the correlation value between the time history of that pixel and that of the reference pixel (indicated with a red cross in each correlation map). Overlaid in blue is the projection of the separatrix at two toroidal locations. Correlation regions appear as filamentary structures approximately field aligned with  $L_{\text{pol}} \ll L_{\parallel}$ . Correlations above random are observed for over a toroidal turn for inner leg filaments and for about half of a toroidal turn for outer leg filaments.  $L_{\parallel}$  is on the order of

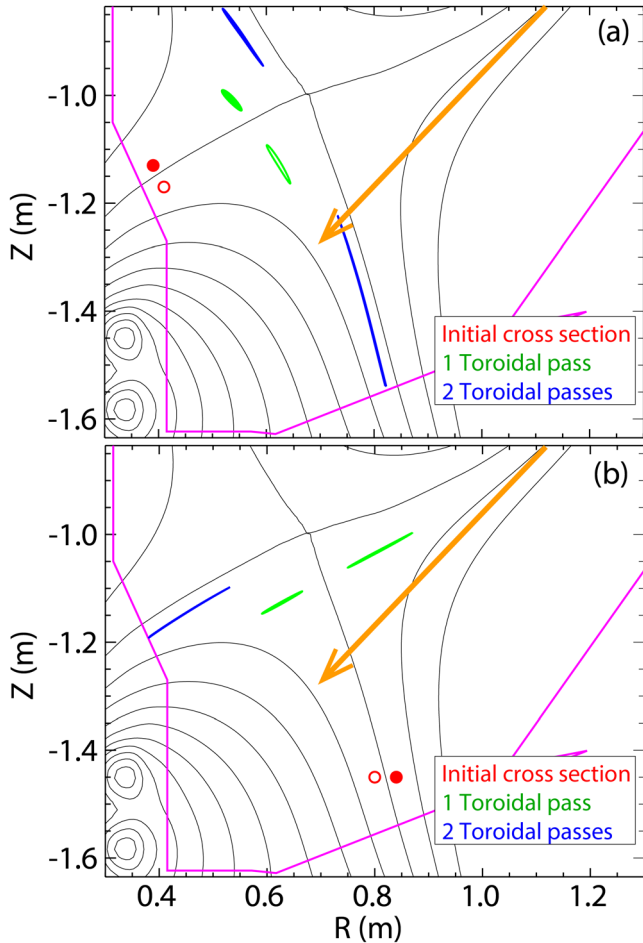


**Figure 10.** Field line mapping of flux tubes in the divertor SOL (filled) and private flux region (empty) of the inner (top) and outer (bottom) leg. Initial flux tubes are in red.

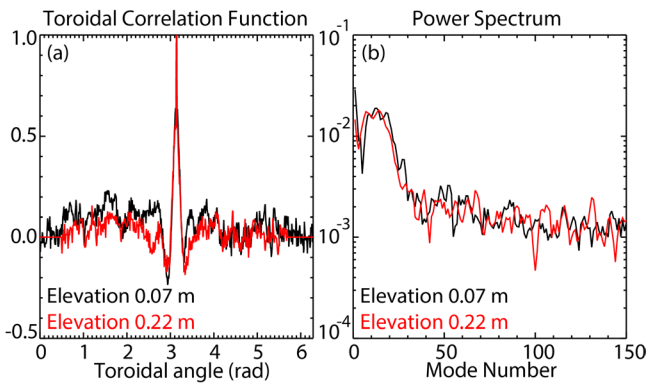


**Figure 11.** (a) Toroidal correlation function for outer leg filaments at two elevations 7 (black) and 22 cm (red) and (b) their toroidal mode number spectrum.

a few meters ( $\sim 2\text{--}3$  m) for both inner and outer leg filaments (the latter being possibly limited by the extent of the C III emission shell). No correlation is observed between inner and outer leg filaments.

The poloidal projection of the 2D cross correlation function along the divertor leg is plotted in figures 9(a) and (b) for outer and inner leg filaments, respectively, as a function of poloidal distance along the leg for a reference pixel

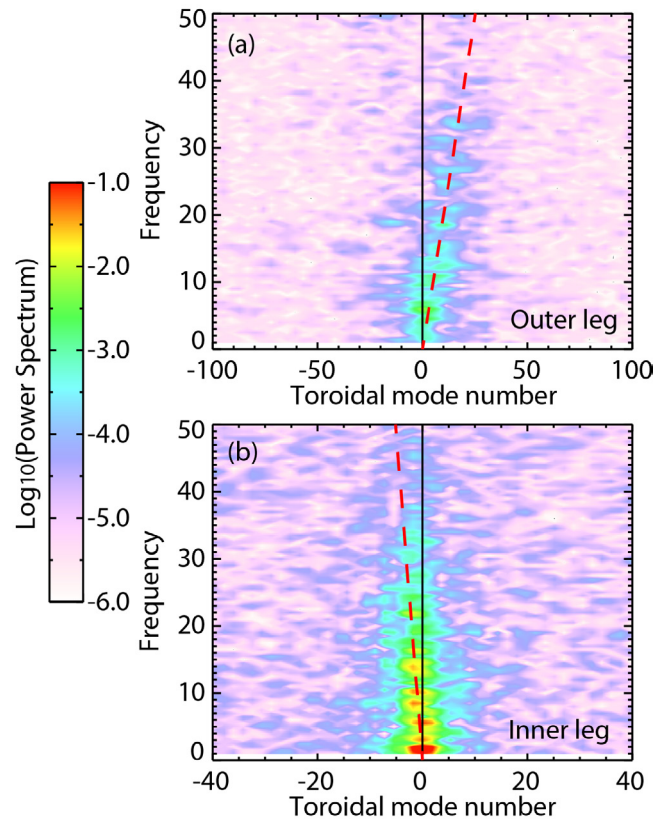


**Figure 12.** Power spectra as a function of frequency and toroidal mode number for outer leg (top) and inner leg (bottom) filaments. A reference line approximately through the maxima of the power spectrum is overlaid in red to guide the eye.

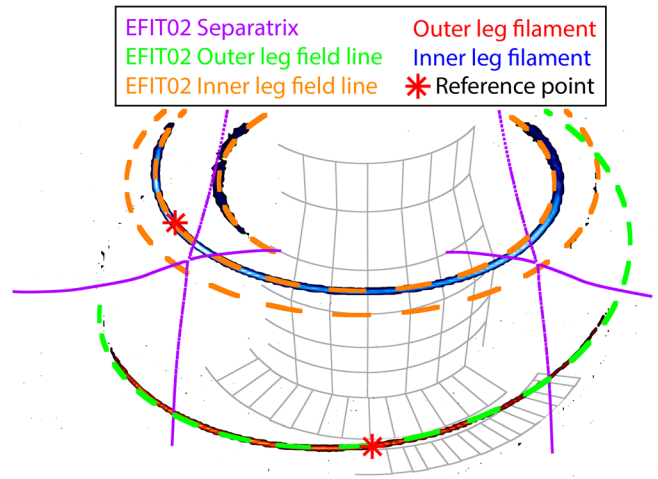


**Figure 13.** 2D cross correlation for an inner (blue) and an outer (red) leg filament. Magnetic field lines from EFIT02 equilibrium reconstruction are overlaid for the inner (orange) and outer (green) divertor.

located at three elevations. Characteristic  $L_{pol}$ , estimated as the FWHM of the cross correlation function, are  $\sim 1\text{--}3.5$  cm for both outer and inner leg. Field-aligned regions of negative correlation (white) are observed in the proximity of the positively correlated regions, leading to partially wave-like poloidal correlation functions (with largest negative correlation values  $\sim -0.2$ ). Figure 9(c) shows the poloidal correlation

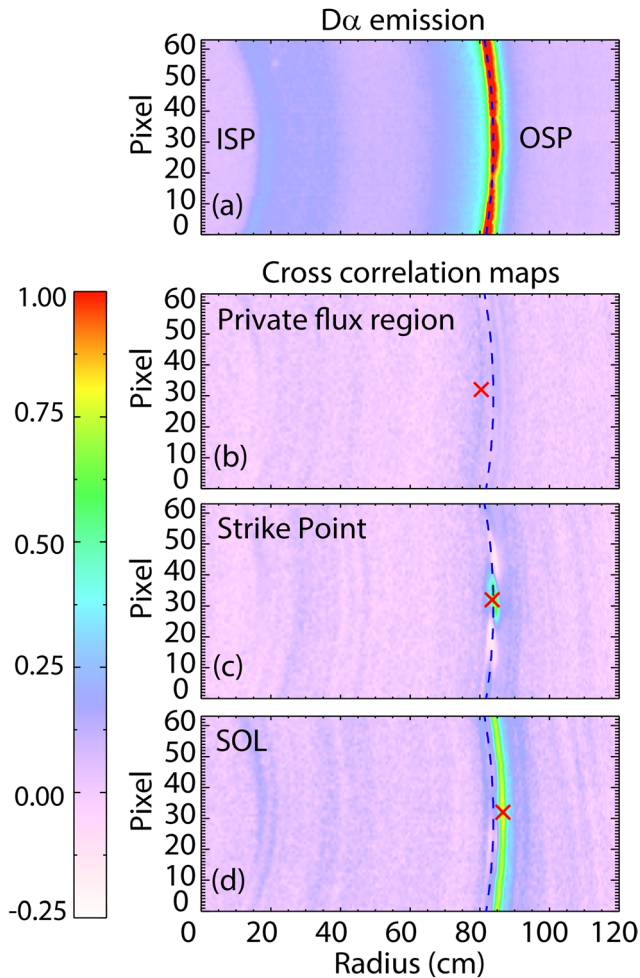


**Figure 14.** (a) Normalized  $D_\alpha$  emission from the lower divertor; 2D cross correlation functions with starting point in (b) private flux region, (c) outer strike point and (d) SOL.

length as a function of elevation from the divertor strike points for outer (black) and inner (red) leg filaments. For outer leg filaments,  $L_{\text{pol}}$  decreases moving the starting pixel upward along the divertor leg and for increasing parallel distance along the region correlated with a single pixel. For inner leg filaments,  $L_{\text{pol}}$  are observed to increase moving the starting pixel poloidally upward along the divertor leg.

The difference in the  $L_{\text{pol}}$  profile for inner and outer leg filaments in figure 9(c) is consistent with the expected squeezing of a flux tube due to the X-point shear [13]. Given the camera setup, flux tube squeezing is expected to happen along the viewing direction for outer leg filaments and across the viewing direction for inner leg filaments. This is illustrated in figure 10, where the field line mapping of a circular flux tube is carried out in the inner and outer divertor leg SOL (filled) and private flux region (empty). The initial circular flux tube is shown in red, subsequent crossings after full toroidal turns are shown in green and blue. The viewing direction is also overlaid in orange.

The 2D correlation map is interpolated onto a toroidal projection at a given elevation along the leg, created with the synthetic diagnostic, to evaluate toroidal mode numbers. Figure 11 shows the toroidal projection of the 2D correlation function (a) as a function of toroidal angle for two elevations along the

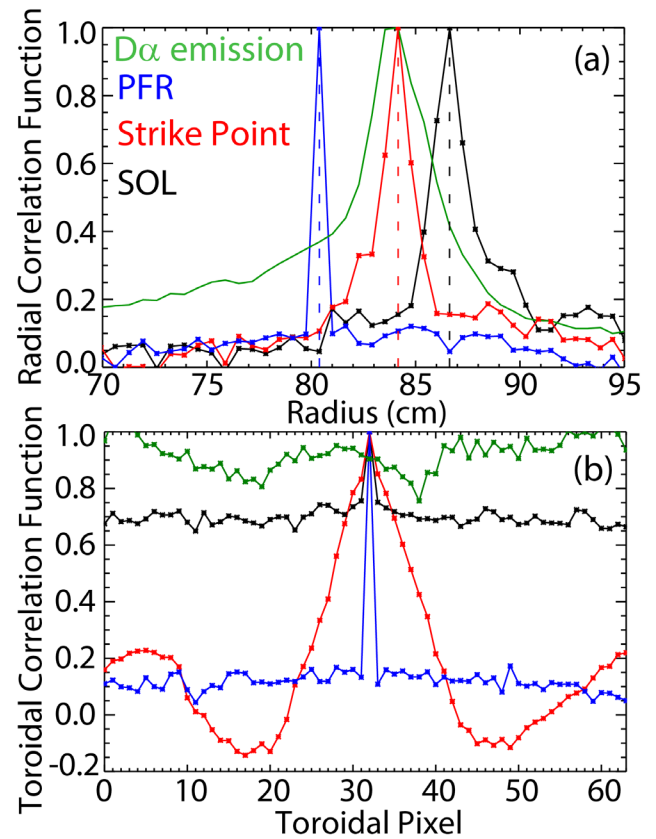


**Figure 15.** (a) Radial and (b) toroidal profiles of cross correlation functions from the top-down  $D_\alpha$  view.

divertor leg (7 and 22 cm) and the mode number power spectrum for  $f \geq 7$  kHz (b), obtained from its FFT. The toroidal correlation function has a partial wave-like correlation structure with an effective toroidal mode number  $\sim 10$ –30. Contour plots of power spectra as a function of frequency and toroidal mode number are shown in figure 12(a) for outer leg filaments and in figure 12(b) for inner leg filaments, obtained from the 2D FFT of the raw emission data interpolated onto a toroidal projection. Lower effective toroidal mode numbers (2–10) are observed for filaments in the inner leg.

### 5.2. Radial filament structure and localization

Radial localization of the filaments is important to assess the mechanisms of filament destabilization (e.g. curvature drive). The assumption of field-alignment of the fluctuations can be exploited to determine their radial location. Figure 13 shows the 2D correlation regions for an inner (blue) and an outer (red) leg filament from C III emission. Magnetic field lines from the EFIT02 reconstruction are overlaid for both the inner divertor (orange) and the outer divertor (green). The radial location of the field line was adjusted to obtain agreement between the correlated region and the projected field line. Inner leg filaments were identified to extend into the private flux region while the purely radial view did not allow localization of outer leg filaments to the private or common flux region within the uncertainty due equilibrium reconstruction and the synthetic diagnostic.

The top-down camera view ( $D_\alpha$  emission, see figure 3) was therefore used to provide complimentary information for the radial localization of the outer leg filaments. Figure 14(a) shows the time-averaged  $D_\alpha$  emission near the lower divertor plate: the outer strike point emission is located at  $R \sim 85$  cm and the inner strike point emission on the angled section of the center stack is projected to  $R \sim 20$  cm on the divertor floor. The radii used here are quoted for the vertical pixel at the center of the view. 2D cross correlation maps from the top-down view are shown in figures 14(b)–(d), moving the reference pixel radially from the private flux region (b), to the strike point (c) and the SOL (d). The value of each pixel in the correlation maps ( $256 \times 64$  pixels) represents the correlation value between the time history of that pixel and that of the reference pixel (indicated with a red cross in each correlation map). The outer strike point position, as inferred from the peak  $D_\alpha$  is overlaid with a blue dashed line.

In the private flux region (figure 14(b)), no correlation structures above the random correlation level are observed. In the few pixels radially localized around the outer strike point (figure 14(c)), the spatial correlation function is both toroidally and radially localized with a partial wave-like pattern in the toroidal direction. Negative correlation regions (white) are observed toroidally nearby the positive correlation region. This correlation structure corresponds to the footprint of the divertor leg filaments observed in C III emission from the radial-downward view (see the footprint of the blue flux tubes rendered in figure 1(c)), indicating the connection of these filaments to the divertor target. No more than a single filament is observed radially at a given toroidal location and negatively correlated regions are not observed in the radial direction. In the SOL (figure 14(d)), correlation regions are helical in shape. This shape is characteristic of upstream turbulence connected to the divertor target, as described in [1] (also see footprint of red flux tubes in the rendering in figure 1(c)). The difference in the shape of the fluctuating structures indicates the physical separation of these different turbulence phenomena in the radial direction.

Radial and toroidal correlation functions are derived interpolating the 2D correlation maps in figure 14 onto radial and toroidal projections. Radial and toroidal profiles of the correlation function of  $D_\alpha$  fluctuations at the divertor target plate are shown in figures 15(a) and (b), respectively. Correlation functions are plotted for a reference point (dashed line) in the private flux region (blue), in the SOL (black), and for a reference point associated with a toroidally localized correlation function (red), corresponding to the cases shown in figures 14(b)–(d). The normalized radial and toroidal profile of  $D_\alpha$  emission is overlaid in green. Pixels that show toroidally-localized correlation functions are radially localized at the peak of the  $D_\alpha$  emission profile, which is representative of the peak incident particle flux and can be associated with the separatrix location.  $L_{\text{rad}}$ , estimated from the FWHM of the radial correlation function, is  $\sim 2$  cm and is comparable to  $L_{\text{POL}}$  and to the radial scale length of the divertor plasma parameters. Correlation functions for turbulent fluctuations in the SOL are uniform along the spiral mapped onto the divertor. Overall, both inner and outer divertor leg fluctuations are localized to

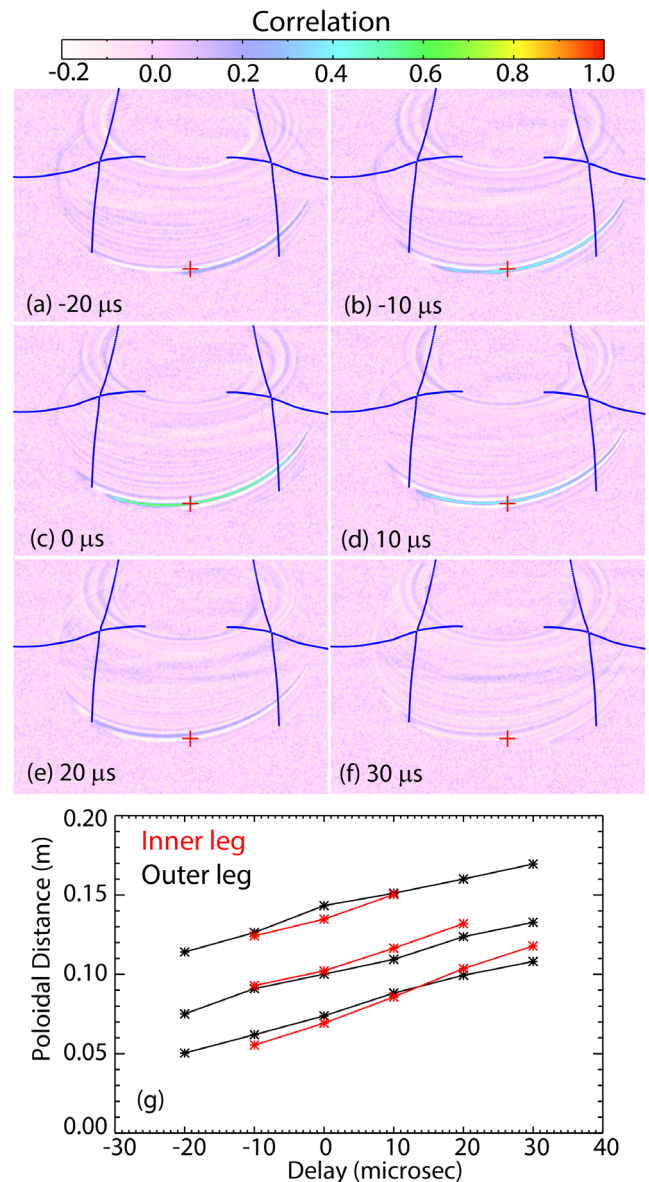


**Figure 16.** ((a)–(f)) Contour plots of 2D correlation functions for outer leg filaments at different delays. (g) Poloidal location of the maximum of the cross correlation function for outer and inner leg filaments as a function of delay.

the bad curvature side (outward in  $R$ ) of the divertor legs and radially limited to the proximity of the separatrix.

## 6. Filament motion

The average turbulence motion is evaluated from the time-delayed cross correlation of a single pixel with every other pixel in the image. Time-delayed cross correlations are performed for both inner and outer leg filaments and for both the radial-downward view and for the top-down view.

### 6.1. Poloidal filament motion

Time delayed cross correlations from the radial-downward view are used to determine the filaments poloidal/toroidal

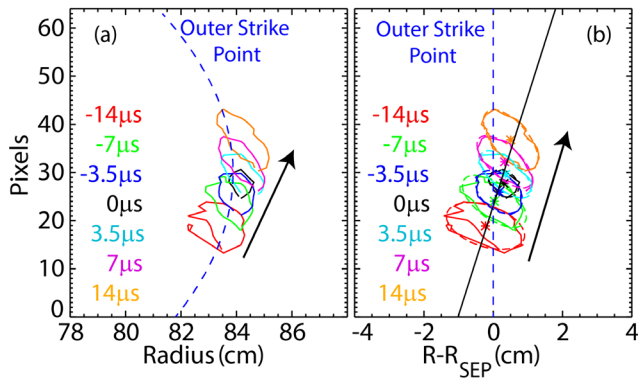


**Figure 17.** Contours of the 2D cross correlation function for different delays (from  $-14$  to  $14 \mu\text{s}$ ) from the top-down view monitoring D- $\alpha$  emission for an outer leg filament.

motion. Figure 16 shows contour plots of the 2D cross correlation maps for an outer leg filament with 6 different delays ( $-20, -10, 0, 10, 20, 30 \mu\text{s}$ ). The reference point at zero-delay is indicated with a red cross. An apparent upward propagation (towards the X-point) is observed for both the outer leg filaments and the inner leg filaments (not shown). The 2D correlation maps are interpolated onto a poloidal projection in the synthetic diagnostic at the toroidal location of the reference pixel. Figure 16(g) shows the poloidal location of the maximum of the correlation function for outer and inner leg filaments as a function of delay. The average propagation velocity is estimated from the linear fit of the poloidal position as a function of delay. Velocities on the order of  $1\text{--}2 \text{ km s}^{-1}$  are observed on both legs. Given the opposite field line helicity on the inner and outer divertor legs, the observed poloidal motion towards the X-point is equivalent to opposite toroidal rotation for inner and outer leg filaments: in the co-current direction for the inner filaments and in the counter-current direction for the outer filaments. The apparent poloidal propagation of outer leg filaments is in the opposite direction of the propagation typically observed for midplane filaments on the low field side SOL (poloidally downward) in NSTX. The footprints on the divertor plate of midplane and divertor-localized filaments (spirals and spots, as in figure 1(c)) therefore rotate in opposite directions in the lower divertor.

### 6.2. Radial filament motion

Time delayed cross correlations from the top-down view are used to determine the filaments radial motion from the motion of their footprint. In figure 17(a), contour plots of the 2D cross correlation function are shown for an outer leg filament with 7 different delays (from  $-14$  to  $14 \mu\text{s}$ ). The contours represent the 70% of the maximum correlation at each delay. The main propagation is toroidal with a finite radial motion. The same contours are fitted with ellipses and plotted versus radial distance from the strike point in figure 17(b). The radial velocity is estimated from the evolution of radial location of the ellipse center. Radial velocities are on the order of  $0.25 \text{ km s}^{-1}$ .

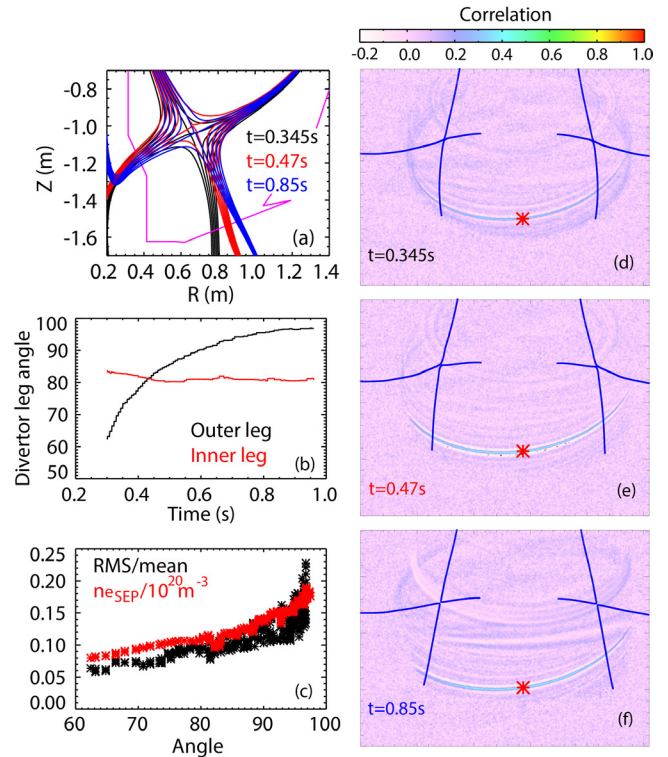


**Figure 18.** (a) Magnetic equilibria for discharge 204963, time evolution of divertor leg angle (b), fluctuation levels and upstream separatrix density (c), ((d)–(f)) 2D cross correlation functions for the three leg angle positions in (a).

## 7. Correlation with outer midplane turbulence

Cross correlation analysis with outer midplane turbulence was carried out to confirm the disconnection between outer leg filaments and upstream turbulence. Passive imaging of the LFS midplane D- $\alpha$  emission was used in NSTX-U for the evaluation of midplane SOL turbulence. Field-aligned intermittent structures are observed in the passive D- $\alpha$  images. Cross correlation of the time series of every pixel in the outer midplane D- $\alpha$  view with every pixel in the radial downward divertor C III view was performed at zero delay (for a total of  $64 \times 80 \times 272 \times 192$  cross correlations). For each pixel in the GPI view the maximum in the correlation value over the entire divertor view ( $272 \times 192$  pixels) was taken. No significant correlation was observed, with a peak value of 0.3 just outside the separatrix. This is to be compared to the typical correlation observed for SOL filaments which is up to 0.8 [1]. The region in the lower divertor associated with the largest correlation value upstream corresponded to the axisymmetric divertor strike point and was therefore indicative of residual coherent plasma motion or axisymmetric particle fluxes.

## 8. Scaling of filament characteristics

Divertor leg filament characteristics were investigated in a series of 13 discharges with comparable low  $\delta$  shape,  $P_{\text{NBI}} \sim 1\text{--}4 \text{ MW}$ ,  $\bar{n}_e \sim 1\text{--}5 \times 10^{15} \text{ cm}^{-2}$  in L-mode regimes. Filaments on the outer leg were always observed in lower

single null and double null even with a small upward bias ( $\delta_{r-sep} > 0$ ). Filaments on the inner leg were observed in lower single null and lower divertor biased double null discharges and disappeared when the double null had any upward bias. Fluctuations spatial scales and dynamics only showed small variability in the discharges in the database. Propagation was consistently towards the X-point on the outer leg with a decreasing velocity as the upstream  $n_e$  ramped during the discharge. Propagation of inner leg filaments reversed direction through the discharge: directed towards the target in the low  $n_e$  early phase and directed towards the X-point and with increasing speed as the discharge progressed. Filaments observed before the reversal appeared to have a shorter parallel extent.

Discharges in the database were used to investigate the effect of leg geometry (divertor leg poloidal length  $L$  and angle  $\alpha$  with respect to the target plate surface on the common flux region side) on the structure of divertor leg filaments. In the magnetic configurations of NSTX-U L-mode discharges, no variation of the inner divertor leg length ( $\sim 30$  cm) and angle ( $\sim 85^\circ$ ) were available. A natural scan of the outer strike point radius was generally carried out through the time evolution of the discharges. Given the nearly fixed X-point position, this resulted in a scan of the divertor angle from  $60^\circ$  to  $100^\circ$ . The evolution of the equilibrium is shown in figure 18(a) for discharge 204963 at 3 times while figure 18(b) shows the temporal evolution of the divertor leg angle for both inner and outer divertor legs. Contour plots of the cross correlation function carried out at a constant elevation for the three different divertor leg angles are shown in figures 18(d)–(f). Similar fluctuating structures are observed in the three configurations. As a function of the divertor angle, no significant change in  $L_{POL}$  or  $L_{RAD}$  was observed. A decrease in poloidal propagation velocity and an increase in the fluctuation level was found but could not be separated from the effect due to the concomitant increase in upstream  $n_e$  (figure 18(c)). No change was seen in the radial localization of the fluctuations with respect to the separatrix as identified from the D- $\alpha$  emission.

## 9. Discussion

Main experimental observations are summarized below:

- Intermittent field-aligned filamentary structures localized to the divertor are observed on the bad curvature side of inner and outer divertor legs.
- Divertor filaments are connected to the divertor plate.
- Characteristic frequencies are  $\sim 10$  kHz and  $\sim 20$ – $30$  kHz for inner and outer leg filaments, respectively.
- $L_{POL} \sim 1$ – $3.5$  cm  $\sim L_{RAD} \sim 2$  cm,  $L_{\parallel} \sim 2$ – $3$  m.
- Toroidal mode numbers are  $\sim 10$ – $30$  and  $2$ – $10$  for outer and inner leg filaments, respectively.
- Inner and outer leg filaments are not correlated.
- Divertor filaments and midplane blobs are not correlated.
- Inner and outer leg filaments propagate towards the X-point with poloidal velocities  $\sim 1$  km  $s^{-1}$ .
- Outer leg filaments propagate outwards radially at  $\sim 0.25$  km  $s^{-1}$ .

### 9.1. Comparison with other devices

Divertor leg filaments have been recently observed in MAST [7] and Alcator C-Mod [16]. Spatial and temporal scales were consistent with the NSTX-U measurements, with  $L_{POL} \sim 10$ – $100$   $\rho_i$  and lifetimes  $\sim 10$ – $100$   $\mu s$ . Analysis on MAST was limited to filaments on the inner divertor leg although outer leg filaments were also observed. With  $B \times \nabla B$  towards the lower divertor, propagation for the inner leg filaments, localized in the private flux region, was towards the inner strike point, i.e. away from the X-point. In C-Mod filaments were observed on both inner and outer divertor legs. With  $B \times \nabla B$  towards the lower divertor, filaments were observed only on the inner leg, were localized to the separatrix and the common flux region and propagated away from the inner target and towards the X-point. Filaments deep in the private flux region were less commonly observed and propagated towards the inner strike point. Outer leg filaments were only observed with  $B \times \nabla B$  in the unfavorable direction and propagated towards the X-point. While spatial and temporal scales were comparable among the devices, occurrence, localization and propagation are still not understood.

### 9.2. X-point disconnection

Results presented in this paper are qualitatively consistent with conjectures on filament disconnection due to the deformation of fluctuating structures near the X-point resulting from magnetic shear [13]. The shape of the divertor filaments ( $L_{POL} \sim L_{RAD}$ ) suggests their generation in the divertor, since flux expansion and magnetic shear would stretch a flux tube with circular cross section at midplane into a ribbon-like structure in the divertor (figure 1).  $L_{POL}$  decreased moving upward along the divertor leg for outer leg filaments and increased along the divertor leg for inner leg filaments, consistently with flux tube squeezing due to X-point shear (figure 10).

The limited  $L_{\parallel}$  for inner leg filaments (i.e. absence of correlation with outer leg fluctuations) and the absence of correlation of outer leg filaments and outer midplane turbulence indicated that these structures do not propagate across the X-point and into the main chamber. Field line mapping of flux tubes representative of divertor leg fluctuations in the LFS common flux region results in highly elongated structures upstream due to the large magnetic shear (from 1 cm radius to elliptical structures 1 m and 0.1 mm in cross section). The flux tube deformation would lead to the radial wavenumber becoming large compared to the inverse  $\rho_i$  and to the dissipation of the perturbation [20].

In the common flux region of the outer divertor, radial separation is observed between divertor leg filaments (observed at the separatrix location) and filaments due to midplane blobs, consistent with the disconnection of midplane turbulence from the divertor target in the very proximity of the LCFS.

### 9.3. Interpretation of experimental observations via multi-fluid modeling

Simulations with the multi-fluid edge transport code UEDGE [34] were performed to help interpret divertor filament

characteristics in the absence of local measurements of plasma parameters. The UEDGE simulations are used in this section to calculate background plasma parameters for theory estimates and code simulations and to understand filament propagation with respect to the local cross field drifts.

Due to the nature of the steady-state UEDGE solution, this method can only estimate time-average quantities and therefore neglects the effect of fluctuations on the dynamics of the filaments. Additionally, turbulence-averaged upstream profiles are used. The non-Maxwellian character of SOL turbulence and the non-linear transport equations and atomic rate coefficients can limit the accuracy of fluid codes in describing experimental results [35, 36]. These effects might be less important for divertor leg turbulence than at the outer midplane due to the low intermittency character of this turbulence and the low fluctuation level (up to 10%–20%).

UEDGE was run on a balanced double null grid ( $24 \times 110$  radial and poloidal cells) generated from the lower half of an EFIT02 reconstruction with the inclusion of the full cross field drifts model. The simulations were constrained by upstream kinetic profiles ( $T_e$ ,  $n_e$ ,  $T_i$ ), LFS midplane D- $\alpha$  emissivity and lower divertor D- $\alpha$  brightness. Poloidally-uniform diffusive radial transport coefficients were derived matching midplane profiles.

Figures 19(a)–(d) shows contour plots of the results of the UEDGE simulations for  $T_e$ ,  $T_i$ ,  $n_e$  and poloidal component of the  $E \times B$  drift velocity. Radial plasma parameters at the divertor plate are plotted in figures 19(e) and (f) for both outer and inner divertor leg. On the low field side SOL,  $E \times B$  velocity is directed towards the target (red contour values). The drift direction reverses approaching the separatrix and into the private flux region where it is directed away from the outer divertor target and into the inner divertor target plate.  $E \times B$  velocities are on the order of  $1 \text{ km s}^{-1}$  in the outer leg towards the X-point and  $0.2\text{--}0.5 \text{ km s}^{-1}$  away from the X-point in the private flux region of the inner divertor leg.

Based on the UEDGE solution,  $\rho_i$  in the proximity of the divertor plates can be estimated to be  $\sim 0.6 \text{ mm}$  in the outer leg and  $0.15 \text{ mm}$  in the inner divertor leg. Local  $\beta$  is on the order of  $3 \times 10^{-4}$  and of  $2 - 3 \times 10^{-5}$  on the outer and inner divertor legs. Parallel velocities into the divertor target are  $\sim 10\text{--}15 \text{ km s}^{-1}$  at the outer strike point and  $5\text{--}8 \text{ km s}^{-1}$  at the inner strike point. The characteristic density SOL width  $l$ , estimated as the FWHM of the  $n_e$  profiles at the target, is  $\sim 4 \text{ cm}$  for both legs. The incident separatrix angle  $\alpha$  is  $\sim 80\text{--}85^\circ$  for both legs. Divertor leg length  $L$  is  $55 \text{ cm}$  for the outer leg and  $30 \text{ cm}$  for the inner leg. The ratio of toroidal to poloidal magnetic field is  $\sim 10$  and  $6$  for inner and outer divertor legs.  $L_{\text{POL}}$  is therefore  $\sim 30 \rho_i$  and  $100 \rho_i$  for outer and inner leg filaments. It should be noted that this is an upper estimate of  $L_{\text{POL}}$  as the effect of poloidal motion is not included ( $v_{\text{pol}} \times \Delta t \sim 0.9 \text{ cm}$  versus  $L_{\text{pol}} \sim 1.5\text{--}3.5 \text{ cm}$ ). The experimental poloidal propagation in the outer leg is on the order of  $1\text{--}2 \text{ km s}^{-1}$ . This is in the same direction and of the same magnitude of the local  $E \times B$  drift velocity derived from UEDGE simulations. On the inner leg, the filaments velocity is  $1\text{--}2 \text{ km s}^{-1}$  generally towards the X-point and thus in opposite direction with respect to the simulated  $E \times B$  drift velocity.

#### 9.4. Comparison with instability theories

Experimentally, divertor leg filaments were observed on the bad curvature side of both divertor legs, indicating a possible curvature-driven mechanism. Drift-wave and interchange modes are responsible for midplane edge/SOL turbulence in tokamaks and instabilities in simple magnetized toroidal configurations (e.g. TORPEX [37], Helimak [38]) and could be playing a role in the generation of divertor leg filaments. In particular, while collisionality can greatly differ, the geometry of devices such as TORPEX and Helimak (open helical field lines connected to end plates without any plasma on closed field lines) can be similar to the divertor leg geometry, relative to turbulence generated locally on the divertor legs. These considerations motivated simulations performed with the ArbiTER code with a resistive-ballooning model on a grid limited to the divertor legs and presented in section 9.5.

Work by Cohen and Ryutov [19, 21] discussed the possibility of sheath-driven divertor instabilities. The experimental filament properties in NSTX-U can be compared with this theory using parameters derived from the UEDGE simulations. The derivation of sheath instabilities assumes radial  $\nabla T_e$  to be the dominant gradient. This is the case for the NSTX-U outer leg while in the inner leg  $\nabla n_e$  is the dominant gradient. Long divertor leg assumptions ( $L \gg l$ ) are satisfied and the approximation of zero tilt of the separatrix with respect to the normal to the divertor plate is appropriate. From the discussion in section 9.3,  $k_{\text{pol}}\rho_i$  is  $\sim 0.06$  and  $0.015\text{--}0.02$  for outer and inner leg filaments, respectively, with  $k_r \sim k_{\text{pol}}$ . Based on the theory from Cohen and Ryutov and following equation (30) in [21], characteristic sheath-instability frequencies are  $\sim 30\text{--}60 \text{ kHz}$  for outer leg and of  $4\text{--}30 \text{ kHz}$  for inner leg filaments. Scale lengths of fluctuations observed in NSTX-U would correspond to the long wavelength branch of sheath instabilities discussed in [20]. Experimental wavenumbers on inner and outer leg are close to those expected for maximum growth rate for the long wavelength branch ( $k\rho_i \sim 0.1$  on the outer leg and  $k\rho_i \sim 0.06$  on the inner leg), which also corresponds to  $k_{\text{pol}} = k_r$ .

In NSTX-U, the presence of filaments did not depend on the incident angle, which is generally expected to be a destabilizing factor for sheath instabilities. However, evaluation of their dispersion relation (equation (34) in [20]) for NSTX-U, with  $k_{\text{pol}} \sim k_r$ , indicates that small angle variations around the normal to the divertor target should not play a significant role. Evaluation of the real part of dispersion relation indicates that on both legs the phase velocities of the long wavelength mode can be on the order of the local drift velocities. This could possibly explain the different propagation observed on inner and outer leg in the laboratory frame and the propagation reversal observed during the discharge on the inner leg.

#### 9.5. Comparison with ArbiTER simulations

The ArbiTER (arbitrary topology equation reader) code [39] was used to understand the possible drivers for divertor leg modes and the disconnection of midplane turbulence from the divertor target. ArbiTER is an eigenvalue solver for linear

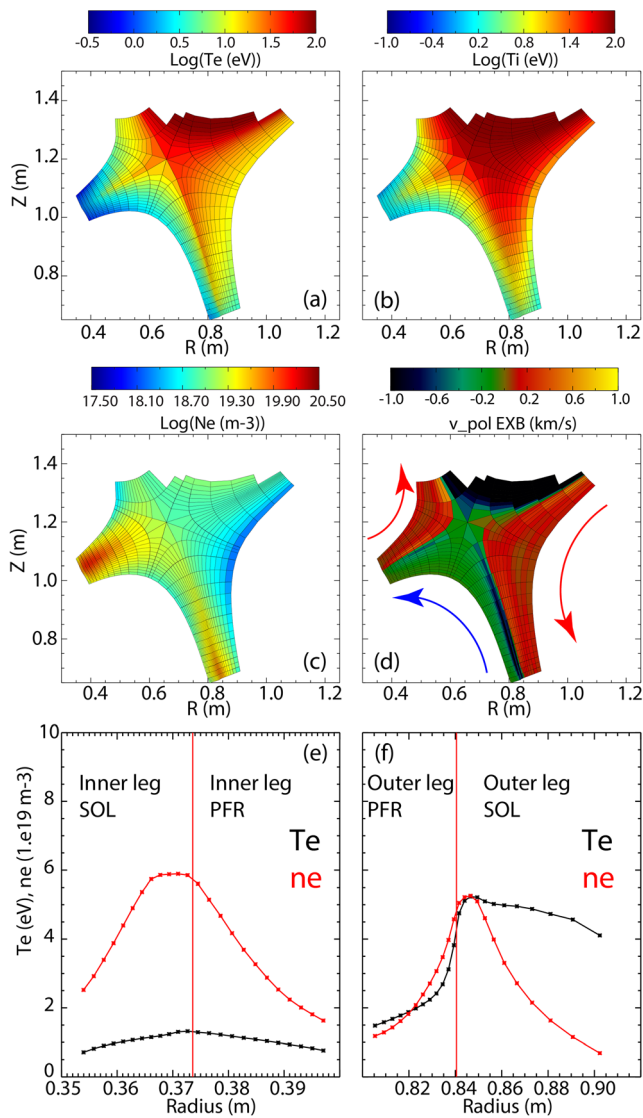


**Figure 19.** UEDGE parameters for NSTX-U discharge 205020: (a)  $T_e$ , (b)  $T_i$ , (c)  $n_e$ , (d) poloidal component of the  $E \times B$  drift, radial profile of  $T_e$  and  $n_e$  at the inner (e) and outer (f) divertor leg.

edge plasma physics problems based on the SLEPC [40] eigen-solver package. The ArBiTER flexible topology makes it ideal to study instabilities in X-point geometry configurations. In order to simulate filamentary structures using a linear code, the assumption is made that such a structure can be represented as a superposition of a toroidally symmetric perturbation of the density profile with a toroidally asymmetric instability. The density profile is perturbed with a Gaussian perturbation a short distance outside the separatrix, creating a region of strong  $n_e$  gradients. The ArBiTER output is processed to identify the fastest growing eigenmode that is localized near this strong  $n_e$  gradient region. The model used for the instability is a three-field resistive-ballooning model. In this model, instability is driven by the interaction of  $n_e$  gradients with curvature. The model equations can be found in [39].

Background plasma profiles for the ArBiTER simulations are based on the upstream experimental plasma profiles and a parallel variation function derived from fits to the 2D UEDGE solution. The simulation grid is based on the EFIT02

reconstruction for discharge 205020. A study was performed using a reduced grid, allowing an increase in the radial resolution. The grid extended only between the X-point and divertor plate (both private and common flux regions) without including any SOL facing plasma on closed field lines. Grids were constructed separately for the inner and the outer divertors. The grid geometry was justified by the divertor localization of the filaments and the absence of correlation between inner and outer leg filaments. Sheath boundary conditions at the divertor plate and conducting boundary conditions at the X-point were utilized. In both divertor legs, modes localized on the bad curvature side of the leg were identified. The instability was driven by the interaction of density gradients with geodesic curvature. Normal and geodesic curvature have effects with the same sign so, while most of the instability drive comes from geodesic curvature, the existence of the instability is correctly predicted looking only at normal curvature. Scans in toroidal mode numbers were performed to map growth rates of these instabilities. Outer leg modes show growth rate saturation for higher mode numbers than inner leg modes, in qualitative consistency with experimental observations.

The ArBiTER code was also used to investigate the parallel connection of midplane instabilities to the divertor target. For these simulations a grid using the full NSTX-U geometry from discharge 205020 was employed, with the same experimental-based profiles already discussed. A perturbation to the density profiles at midplane was employed and linear simulations were performed with the resistive-ballooning model discussed earlier and compared at toroidal mode number  $n = 15$ . The degree of connectivity between eigenmodes localized near the outboard midplane and the divertor plate was quantified with the following approach. Consistent with the numerical eigenmode solution, the mode structure was assumed to be flat in the parallel direction until the X-point and to exponentially decay in the divertor leg. The density perturbation at the outer divertor plate was compared to the density perturbation at the outboard midplane to evaluate a divertor connection length for the instability. If a mode falls off exponentially, the characteristic decay length  $\lambda$  as a fraction of total length  $L$  can be written as  $\lambda/L = -1/\log(\delta n_{\text{div}}/\delta n_{\text{mid}})$ . This ratio of the mode connection length to the total connection length is used to quantify the degree of connectivity. In the proximity of the separatrix, the mode is disconnected by the long divertor leg. The mode connectivity is observed to increase as the mode moves away from the separatrix, with  $\lambda/L$  of 0.1132 at the separatrix increasing to 0.3116 at a flux surface .536 cm further out on the outboard midplane. This is consistent with the experimental observations in section 5, showing a radial separation between divertor localized modes and spirals corresponding to upstream blobs.

## 10. Conclusions

Divertor-localized fluctuations were observed for the first time in NSTX-U discharges via fast camera imaging. Field-aligned filaments connected to the divertor target plate were radially localized to the bad curvature side of each divertor

leg and limited to the region below the X-point. Filaments had  $L_{\text{POL}}$  and  $L_{\text{RAD}}$  of 1–3.5 cm ( $10\text{--}100 \rho_i$ ) and  $L_{\parallel}$  of 2–3 m. Toroidal mode numbers were  $\sim 10\text{--}30$  and  $2\text{--}10$  for outer and inner leg filaments, respectively. Disconnection between inner and outer leg filaments and the absence of correlation with upstream turbulence support the hypothesis of X-point disconnection of divertor leg filaments. Divertor leg filaments were observed to be radially separated from divertor fluctuations due to midplane blobs, indicating the limited penetration of midplane modes in the divertor near the separatrix.

Assessing the role of leg filaments with respect to divertor heat flux spreading near the separatrix is critical given the possible disconnection of midplane turbulence. Visible imaging, as in this paper, can not be directly used for measurements of particle or heat fluxes, since this requires knowledge of the absolute  $n_e$  and/or  $T_e$  fluctuations, along with the local radial fluid velocities (and relative phases). Fluctuation-induced transport measurements are envisioned in the future with Langmuir probes in NSTX-U.

Understanding the spatial and temporal scales of divertor leg fluctuations, as carried out in this paper, is necessary for the development and validation of theoretical models in codes, which in turn can be used to study their impact on heat and particle fluxes. Initial comparisons were presented in this paper with instability theories of sheath instabilities and simulations of resistive-ballooning modes with the ArbiTER code. The latter identified unstable modes in the bad curvature region of the divertor legs with mode numbers in qualitative agreement with the experimental observations.

## Acknowledgments

The authors acknowledge T. Rognlien for assistance with UEDGE, D. Battaglia and D. Mueller for NSTX-U operation, S. Sabbagh for equilibrium reconstruction, A. Diallo, R. Bell, W. Guttenfelder, R. Maqueda for useful discussions. This work was performed under the auspices of the US Department of Energy by Lawrence Livermore National Laboratory under Contract DE-AC52-07NA27344, Princeton University under Contract DE-AC02-09CH11466 and Lodestar Research Corporation under Contract DE-FG02-02ER54678. The digital data for this paper can be found in <http://arks.princeton.edu/ark:/88435/dsp018p58pg29j>.

This manuscript is based upon work supported by the U.S. Department of Energy, Office of Science, Office of Fusion Energy Sciences, and has been authored by Lawrence Livermore National Laboratory under Contract Number DE-AC52-07NA27344, Princeton University under Contract Number DE-AC02-09CH11466 and Lodestar Research Corporation under Contract Number DE-FG02-02ER54678 with the U.S. Department of Energy. The publisher, by accepting the article for publication acknowledges, that the United States Government retains a non-exclusive, paid-up, irrevocable, worldwide license to publish or reproduce the published form of this manuscript, or allow others to do so, for United States Government purposes.

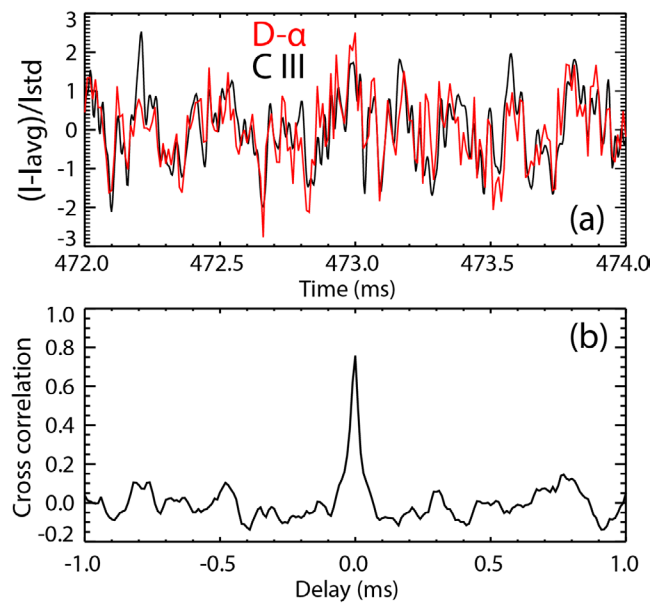


**Figure A1.** (a) Time series of C III (black) and  $D_{\alpha}$  (red) brightness from the inner leg on the two camera views, (b) cross correlation between the two time series.

## Appendix

In NSTX-U attached divertor conditions, C III emissivity was mostly due to electron impact excitation and can therefore be written as  $E_{\text{C-III}} = n_{\text{C}^{2+}} \times n_e \times \text{PEC}_{\text{C III-ex}}$  where  $n_{\text{C}^{2+}}$  is the density of doubly ionized carbon ions and  $\text{PEC}_{\text{C III-ex}}$  is the photon emission coefficient for electron impact excitation (mostly a function of  $T_e$ ). The fluctuating C III emissivity can thus be due to a combination of fluctuations in  $n_e$ ,  $n_{\text{C}^{2+}}$  and  $T_e$ . Figure A1(a) shows time histories of inner divertor leg fluctuations from a pixel in the radial-downward C III view (black) and a pixel, magnetically connected to the C III pixel but toroidally separated, from the D-α top-down view (red). Consistent fluctuating structures are observed in the two diagnostics with zero-delay cross correlation up to 0.75 as shown in figure A1(b). The D-α emissivity can be written as  $E_{\text{D-}\alpha} = n_{\text{D}^0} \times n_e \times \text{PEC}_{\text{D}^0\text{-ex}}$ , where  $n_{\text{D}^0}$  is the deuterium neutral density. The large correlation observed suggests that divertor-localized fluctuations imaged via C III can be mainly representative of  $n_e$  fluctuations, which is the only common factor in the two emissivities. The dependence of the emissivities on other quantities, prevents the direct use of the brightness fluctuation level to represent the  $n_e$  fluctuation level.

## ORCID iDs

Vlad Soukhanovskii <https://orcid.org/0000-0001-5519-0145>  
James Myra <https://orcid.org/0000-0001-5939-8429>

## References

- [1] Maqueda R. et al 2010 *Nucl. Fusion* **50** 075002
- [2] Eich T. et al 2013 *Nucl. Fusion* **53** 093031

- [3] Goldston R. 2012 *Nucl. Fusion* **52** 013009
- [4] Chang C. et al 2017 *Nucl. Fusion* **57** 116023
- [5] D'Ippolito D. et al 2011 *Phys. Plasmas* **18** 060501
- [6] Myra J.R. et al 2016 *Phys. Plasmas* **23** 112502
- [7] Harrison J.R. et al 2015 *Phys. Plasmas* **22** 092508
- [8] Grulke O. et al 2014 *Nucl. Fusion* **54** 043012
- [9] Terry J. et al 2009 *J. Nucl. Mater.* **390–1** 339–42
- [10] Antar G.Y. et al 2005 *Phys. Plasmas* **12** 032506
- [11] Tanaka H. et al 2009 *Nucl. Fusion* **49** 065017
- [12] Myra J.R. et al 2006 *Phys. Plasmas* **13** 112502
- [13] Farina D. et al 1993 *Nucl. Fusion* **33** 1315
- [14] Zweben S.J. et al 2017 *Rev. Sci. Instrum.* **88** 041101
- [15] Walkden N. et al 2017 *Nucl. Fusion* **57** 126028
- [16] Terry J. et al 2017 *Nucl. Mater. Energy* **12** 989–93
- [17] Berk H.L. et al 1993 *Nucl. Fusion* **33** 263
- [18] Berk H.L. et al 1991 *Phys. Fluids B* **3** 1346–54
- [19] Cohen R.H. et al 1996 *Contrib. Plasma Phys.* **36** 161–5
- [20] Cohen R.H. et al 2005 *Plasma Phys. Control. Fusion* **47** 1187
- [21] Ryutov D.D. et al 2004 *Contrib. Plasma Phys.* **44** 168–75
- [22] Cohen R. et al 2007 *Nucl. Fusion* **47** 612
- [23] Menard J. et al 2012 *Nucl. Fusion* **52** 083015
- [24] Persistence of Vision Raytracer Pty. Ltd. [www.povray.org/](http://www.povray.org/)
- [25] Scotti F. et al 2012 *Rev. Sci. Instrum.* **83** 10E532
- [26] Menard J. et al 2017 *Nucl. Fusion* **57** 102006
- [27] Battaglia D.J. et al 2018 *Nucl. Fusion* **58** 046010
- [28] Boyer M.D. et al 2018 *Nucl. Fusion* **58** 036016
- [29] Fenstermacher M.E. et al 1997 *Phys. Plasmas* **4** 1761–73
- [30] Vision Research [www.visionresearch.com/](http://www.visionresearch.com/)
- [31] Andover Bandpass Filters [www.andover.com](http://www.andover.com)
- [32] Interactive Data language (IDL) [www.exelisvis.com/ProductsServices/IDL.aspx](http://www.exelisvis.com/ProductsServices/IDL.aspx)
- [33] Zweben S. et al 2004 *Nucl. Fusion* **44** 134
- [34] Rognlien T. et al 1992 *J. Nucl. Mater.* **196–8** 347
- [35] Krasheninnikov S.I. et al 2009 *Phys. Plasmas* **16** 014501
- [36] Pigarov A.Y. et al 2012 *Phys. Plasmas* **19** 072516
- [37] Furno I. et al 2008 *Phys. Rev. Lett.* **100** 055004
- [38] Li B. et al 2009 *Phys. Plasmas* **16** 082510
- [39] Baver D.A. et al 2016 *Commun. Comput. Phys.* **20** 136–55
- [40] [www.grycap.upv.es/slepc/](http://www.grycap.upv.es/slepc/)